ELSEVIER

Contents lists available at ScienceDirect

Earth and Planetary Science Letters

www.elsevier.com/locate/epsl



Reversible scavenging traps hydrothermal iron in the deep ocean

Saeed Roshan a,b,c,*, Tim DeVries b,c, Jingfeng Wu a, Seth John d, Thomas Weber e



- ^a Rosenstiel School of Marine and Atmospheric Science, University of Miami, Coral Gables, FL, 33146, USA
- ^b Earth Research Institute, University of California, Santa Barbara, CA, 93106, USA
- ^c Department of Geography, University of California, Santa Barbara, CA, 93106, USA
- d Department of Earth Sciences, University of Southern California, Los Angeles, CA 90089, USA
- ^e Department of Earth and Environmental Sciences, University of Rochester, Rochester, NY 14618, USA

ARTICLE INFO

Article history: Received 20 September 2019 Received in revised form 14 April 2020 Accepted 19 April 2020 Available online xxxx Editor: L. Robinson

Keywords: hydrothermal iron dissolved iron US GEOTRACES reversible scavenging numerical modeling

ABSTRACT

Recent studies suggest that seafloor hydrothermal vents could be an important source of iron (Fe) to the surface ocean, stimulating plankton growth and biological carbon export. However, quantifying the supply of hydrothermal Fe to the surface ocean requires accurately modeling its stabilization and removal processes, which are poorly known. Here, we determine the physical speciation of dissolved Fe along an oceanographic transect following a coherent hydrothermal plume that emanates from the East Pacific Rise (EPR) and persists westward over 4.000 km in the Tropical South Pacific. Our observations show that the plume persists horizontally, but descends vertically, and consists primarily of very large Fe colloids. Guided by these observations, we develop a new size-resolved mechanistic model of hydrothermal Fe dispersion in this region, in which the stabilization of hydrothermal Fe is explained by a reversible particulate exchange process. This model accurately captures the lateral dispersion, downward settling and physical speciation of hydrothermal Fe along this transect. An alternate model that uses a hydrothermal source of Fe-binding ligands to facilitate Fe transport within the deep ocean can reproduce the long-range transport of hydrothermal Fe, but does not reproduce the vertical descent of the plume. Our model shows that hydrothermal Fe vented from the EPR is trapped in the deep ocean, and only 1% of this iron ever makes it to the surface where it can stimulate biological productivity. At the global scale, 3-5% of hydrothermal Fe makes it to the surface ocean, the vast majority of which originates from Southern Ocean vents and upwells in the Southern Ocean. Our best estimate of the global supply of hydrothermal Fe to the surface ocean, based on data-constrained estimates of ocean circulation, mantle 3 He venting, and the hydrothermal Fe: 3 He ratio from the EPR, is 0.12 ± 0.07 Gmolyr $^{-1}$. This is about 60-70 times lower than the supply of Fe from aerosol dust deposition, but could be regionally important in the Antarctic zone of the Southern Ocean.

© 2020 Elsevier B.V. All rights reserved.

1. Introduction

Ocean productivity is limited by iron (Fe) in many nutrient-rich ocean regions, such as the Southern Ocean and equatorial and sub-arctic Pacific (Boyd et al., 2007; Moore et al., 2013; Tagliabue et al., 2017). These remote regions receive little of the wind-blown continental dust that constitutes the primary source of Fe to most of the surface ocean, and therefore plankton in these regions rely primarily on Fe from subsurface sources (Tagliabue et al., 2014; Tagliabue and Resing, 2016). Recent studies have demonstrated long-range transport of dissolved hydrothermal Fe in the deep ocean (Resing

E-mail address: saeed.roshan@geog.ucsb.edu (S. Roshan).

et al., 2015; Fitzsimmons et al., 2014, 2017), and models suggest that this iron could provide a significant boost to marine productivity, particularly in the Fe-limited Southern Ocean (Resing et al., 2015; Tagliabue and Resing, 2016).

In this study, we evaluate the transport of hydrothermal dissolved Fe within the deep ocean, and its capacity to reach the surface ocean, by measuring and modeling the physical speciation of dissolved Fe along the GEOTRACES GP16 zonal transect in the Tropical South Pacific (Moffett and German, 2018). The western half of this transect follows a well-known basin-scale Fe plume emanating hydrothermal vents along the East Pacific Rise (EPR; Fig. 1), and offers the first simultaneous observations of hydrothermal Fe in both nearfield and farfield hydrothermal plumes. Iron cycle models have been unable to reproduce the predominantly westward propagation and vertical descent of this hydrothermal

^{*} Corresponding author at: Department of Geography, University of California, Santa Barbara, CA, 93106, USA.

plume (Tagliabue et al., 2016), leaving large uncertainties on the supply of hydrothermal Fe from the EPR to the surface ocean.

Using new observations of the detailed size speciation of dissolved Fe within the hydrothermal plume (Section 3.1), we develop a new model of hydrothermal Fe dispersion. The model predicts that the stabilization and slow settling of hydrothermal Fe is due to reversible scavenging of hydrothermal Fe by sinking organic particles, in which inorganic iron colloids released from hydrothermal vents is gradually transformed to ligand-bound organic Fe in the farfield hydrothermal plume (Section 3.2). The overall effect of the reversible exchange process is to trap hydrothermal Fe released from EPR vents in deep water masses, severely limiting its supply to the surface and confining its impact to the Antarctic region of the Southern Ocean (Section 3.3). When extrapolated globally, our model predicts that only hydrothermal vents from Southern Ocean ridge system can supply significant amounts of hydrothermal Fe to the surface (Section 4). We close by discussing future research avenues that can better constrain the role of hydrothermal Fe sources in the global marine Fe cycle (Section 5).

2. Sampling and analysis

Trace metal samples were collected onboard RV Thompson in the late 2013 in the Tropical South Pacific using the US GEO-TRACES sampling protocol (Moffett and German, 2018; the transect is known as GP16 and the station locations along its western portion are shown in Fig. 1A). Samples were initially filtered through 0.2- µm AcropakTM capsule filters. Aliquots of those filtered samples were ultra-filtered applying a Cross Flow Filtration (CFF) technique on board the ship (Roshan and Wu, 2018). CFF cassettes (cutoff sizes of 5, 10, 30, and 300 kDa) were purchased from PelliconTM and cleaned using 10 L of trace-metal grade nitric acid (HNO₃) with pH 1.5 in a trace-metal clean laboratory before going to sea. Peristaltic pumps and Teflon tubing were used to flush the samples though filters. Each size cutoff filtration was conducted on separately-sub-sampled aliquots. Between samples, the ultrafiltration devices were restored and cleaned using pH \sim 1.5 ultra-clean hydrochloric acid (HCl) (20 min, flow rate = 5 ml min^{-1}), neutralized using deionized water (resistivity = 18.2 M Ω ; 20 min, flow rate $= 5 \text{ ml min}^{-1}$), and preconditioned using the same sample before collection (15 min, flow rate = 5 ml min $^{-1}$). All the trace metal grade acids used in this study were purified using an inhouse all-Teflon distillation unit purchased from SavillexTM. All the filtered (0.2 µm) and ultra-filtered (5, 10, 30, and 300 kDa) seawater samples were stored in pre-cleaned LDPE bottles. After transportation to the inland lab (at the University of Miami), samples were acidified (to pH \sim 1.8) using trace metal grade concentrated HNO₃ and stored at room temperature for at least 2 months prior to analyses.

Total dissolved and ultra-filtered samples were determined for Fe, Mn and Cu concentrations using a magnesium hydroxide (Mg(OH)₂) co-precipitation technique coupled to an inductively-coupled plasma mass spectrometer purchased from Thermo ScientificTM. The efficiency of the co-precipitation step was quantified using an isotope dilution technique for Fe and Cu (i.e., spiking the samples with ⁵⁷Fe and ⁶⁵Cu isotopes before starting the entire process), and a recovery calibration curve technique for Mn (i.e., using ⁵⁷Fe, ⁵²Cr and ⁵⁹Co to construct calibration curves based on standard seawater samples; details can be found in Wu and Boyle (1998) and Wu et al. (2014)). The standard deviation among the replicates (2 or 3) was \sim 0.03 nM for the total dissolved Fe and \sim 0.02 nM for soluble (i.e., ultra-filtrated) Fe. Colloidal Fe concentrations were determined by residual, and assuming independent errors have an uncertainty of \sim 0.035 nM.

3. Results

3.1. Characteristics of the East Pacific Rise hydrothermal Fe plume

The western portion of the GP16 transect follows one of the most distinctive and well-studied hydrothermal Fe plumes in the ocean, emanating from the Southern East Pacific Rise (SEPR) at 2,500 m depth. The primary hydrographic signature of the plume is a core of elevated δ^3 He (Fig. 1A), which results from the input of ³He-rich hydrothermal fluids from active vents along the SEPR (Jenkins et al., 2018). The δ^3 He plume is advected westward with the prevailing currents at this latitude in the deep Southeast Pacific (Stommel, 1982), and extends over 4,000 km (Fig. 1A). Coincident with the plume of elevated δ^3 He is a striking plume of elevated dissolved Fe (Fig. 1B), presumed to originate from the same hydrothermal vents along the SEPR (Resing et al., 2015; Fitzsimmons et al., 2017). However, unlike the ³He plume, which retains its symmetry around the 2,500 m depth horizon as it mixes with the surrounding seawater (Fig. 1A), the core of the dissolved Fe plume becomes deeper with distance from the vent (Fig. 1B).

The features of this hydrothermal Fe plume, including its distal extent and vertical descent, have been described previously (Resing et al., 2015; Fitzsimmons et al., 2017). Here, we expand on the insights of these previous studies by performing multi-cutoff molecular weight-partitioning to reveal the detailed size spectrum of dissolved Fe in the plume, between \sim 2000–3000 m depth (Fig. 2). We find that the size spectrum of dissolved Fe in the plume is bimodal, with almost all dissolved Fe occurring as either large colloids (>300 kDa, where 1 Da = 1 g mol⁻¹) or as truly soluble Fe (<5 kDa) (Fig. 2). We found very little dissolved Fe in the intermediate size classes, suggesting that dissolved Fe in the plume is composed of two very distinct Fe species. The size partitioning of dissolved Fe is coherent throughout the plume, displaying little spatial variation (Suppl. Fig. 2).

We determine that, on average, $73 \pm 15\%$ of the dissolved Fe in the western portion of the GP16 transect occurs in the colloidal size class, >10 kDa (Fig. 1C). This proportion agrees with that determined by Fitzsimmons et al. (2017) for the same transect. The maximum concentration of Fe colloids is offset downward by \sim 400 m from 110° W to 150° W (Fig. 1C; compare the distribution with the horizontal line drawn at 2,500 m), with a distribution very similar to that of total dissolved Fe (Fig. 1B). The smaller and less concentrated species of soluble Fe does not exhibit the same coherence in the plume, but its maximum concentration also appears to be slightly deeper than 2,500 m in the far-field plume (Fig. 1D).

While the detailed size spectrum of dissolved Fe in the hydrothermal plume suggests two distinct dissolved Fe species, it does not reveal the exact chemical composition of the Fe. Comparing the size fractionation of Fe in the plume with that of other metals may shed some light on the chemical characteristics of the hydrothermal Fe species. Thus, in addition to Fe, we also measured the detailed size speciation of manganese (Mn) and copper (Cu) in the hydrothermal plume (Fig. 2). Dissolved Mn occurs almost exclusively as truly-soluble species (Fig. 2), most likely as inorganic Mn(II) (Stumm and Morgan, 1996), and is dispersed away from the hydrothermal vent without descending at all (Suppl. Fig. 3). This indicates that the descent of Fe (including truly-soluble Fe) may reflect some association with organic matter. Copper is completely organic-associated and does not have a hydrothermal source along the GP16 transect (Roshan and Wu, 2018). It also has a bimodal size distribution (Fig. 2) and occurs as \sim 40% large colloids and \sim 60% truly soluble Cu (Roshan and Wu, 2018). Since the type of organic matter that can bind to Cu and Fe appear to be similar (Martell and Smith, 2013; Abualhaija et al., 2015), it is reasonable to infer that some Fe in the plume is also organically-bound. However, the much larger fraction of Fe in the large colloidal phase,

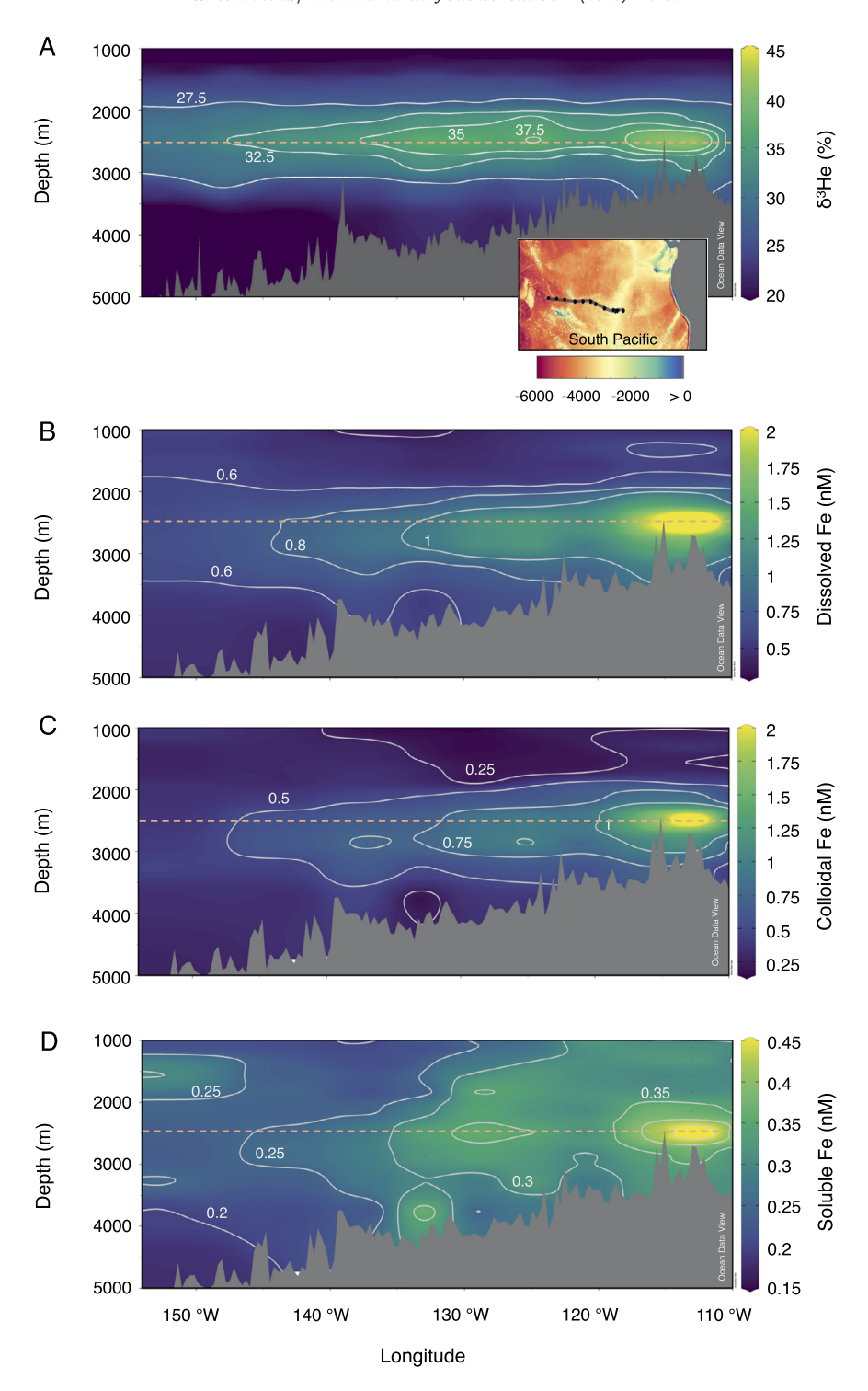


Fig. 1. Measured distributions of (A) δ^3 He (defined as ($(^3\text{He})^4\text{He})_{\text{sample}}/(^3\text{He})^4\text{He})_{\text{air}} - 1)×100)$), (B) total dissolved Fe (<0.2 μm), (C) colloidal Fe (10 kDa – 0.2 μm) and (D) soluble Fe (<10 kDa) along the western portion of the GP16 transect (location shown by black circles and line in the inset plot of panel A). The data has been first binned to the coarse grid of our ocean circulation model and then interpolated using Ocean Data View (Schlitzer, 2016) for comparison with our model results (Fig. 4). See Suppl. Fig. 1 for locations of original measurements. The inset plot in panel A displays a color map of ocean bottom topography with respect to the sea surface in meters (negative downwards). The continuous meridional segment with bottom depth of ~2,500 m (yellowish hue) at the east of the transect shows the location of the Southern East Pacific Rise. Color maps were created using Ocean Data View (Schlitzer, 2016). (For interpretation of the colors in the figure(s), the reader is referred to the web version of this article.)

compared to Cu, suggests that inorganic species also contribute to large Fe colloids. Based on these observations, we hypothesize that large Fe colloids consists of both organic and inorganic phases, while the soluble Fe species are all organic-bound plus some truly-soluble inorganic species.

In all, these observations support the inferences of Fitzsimmons et al. (2017) that Fe emerges as inorganic Fe colloids from hydrothermal vents, and in the farfield is transformed to organic Fe and gradually settles due to reversible exchange with organic particles. Elevated concentrations of soluble Fe in the hydrothermal

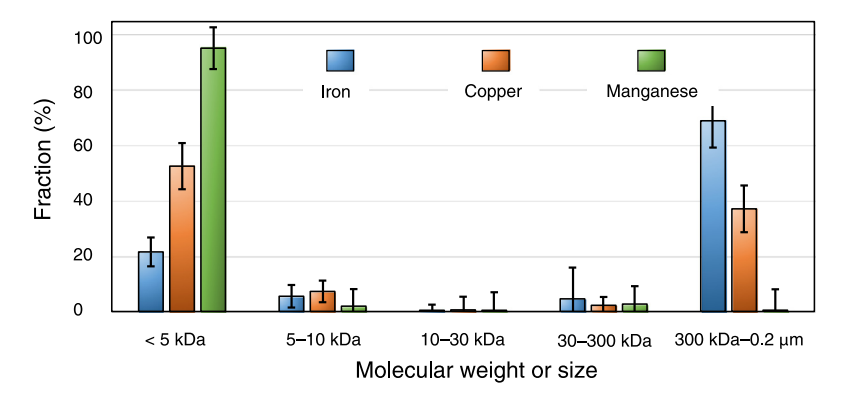


Fig. 2. Fraction of dissolved Fe, Mn and Cu in different molecular weight or size classes. Data are from the core of the hydrothermal plume at 2,200-2,800 m along the western portion of the GP16 transect (Fig. 1A inset). Error bars represent the standard deviation among all the ultra-filtered samples in that depth range.

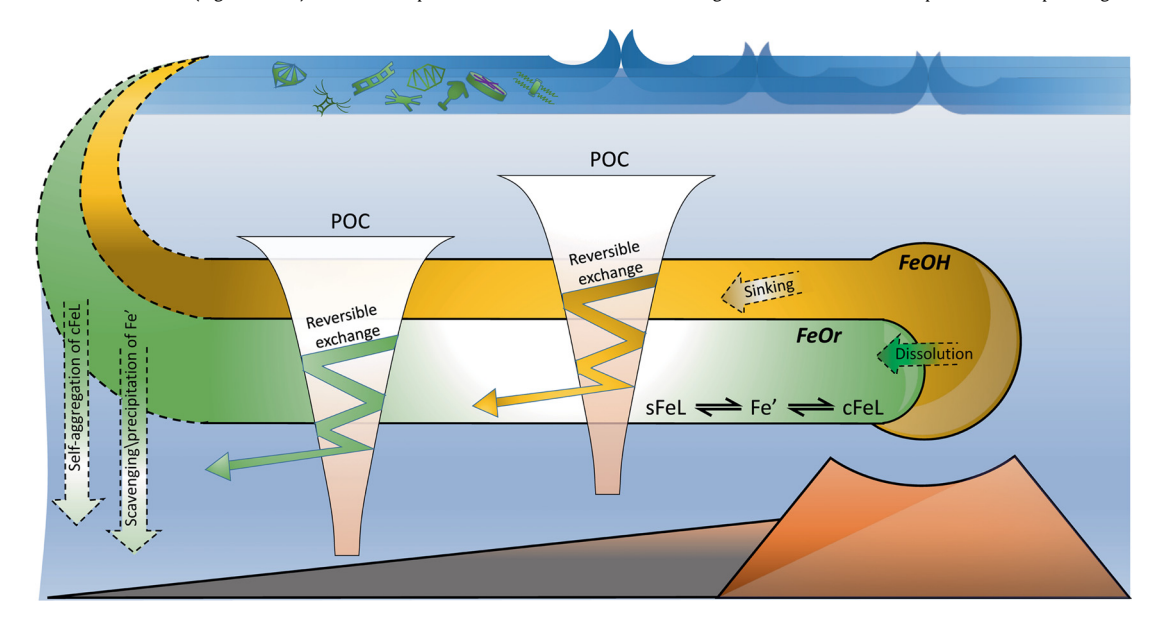


Fig. 3. Schematic of our hydrothermal dissolved Fe model (not to scale). The diagram shows the proposed processes influencing hydrothermal dissolved Fe after its release from vents as iron oxyhydroxide colloids (FeOH). The model simulates both FeOH and organic Fe (FeOT = FeL + Fe' where FeL » Fe') simultaneously. The reversible exchange of FeOH and FeL (the major fraction of FeOr) with sinking particulate organic carbon (POC; shown as funnels) is the main process explaining the distal transport and vertical descent of hydrothermal dissolved Fe, which takes place throughout the ocean. FeOH is also dense enough to sink slowly. Removal of hydrothermal Fe via scavenging and/or precipitation of free Fe' ions, by aggregation of FeL molecules, and by burial of Fe that is adsorbed onto POC also takes place throughout the ocean (represented by downward arrows on the left side of the schematic). Hydrothermal Fe that escapes these fates can be transported to the surface to fuel biological productivity.

plume (Fig. 1D) also clearly support the dissolution of colloidal Fe to soluble Fe. Based on these inferences, we propose a new model of hydrothermal Fe dispersion in Section 3.2.

3.2. A data-constrained mechanistic model of hydrothermal Fe dynamics

Based on the inferences in Section 3.1 we propose a new mechanistic model of hydrothermal Fe cycling, which is illustrated schematically in Fig. 3. In this model, the Fe vented from hydrothermal systems occurs as inorganic Fe colloids. The processes creating these inorganic colloids occur at the subgrid scale and are not explicitly represented in the model. At the subgrid scale, Fe(II) in hot and acidic hydrothermal fluid rapidly oxidizes to insoluble Fe(III) at the initial stages of plume mixing with oxygenated seawater. Insoluble Fe(III) is swiftly converted to inorganic Fe particles (Rudnicki and Elderfield, 1993), with a fraction remaining in the dissolved phase as large colloids. This colloidal Fe is the ultimate source of hydrothermal Fe in our model, and is dense and quasistable without assistance from organic ligands (Yücel et al., 2011; Feely et al., 1996). Following Fitzsimmons et al. (2017), we refer to these inorganic Fe colloids as iron oxyhydroxide (FeOH), since neg-

ligible particulate sulfur can be found in the SEPR hydrothermal plume (FeS is the other major constituent of hydrothermal inorganic iron) (Yücel et al., 2011; Hoffman et al., 2018).

Upon release from hydrothermal vents, these FeOH colloids may persist in the water column as they drift slowly downwards due to their high density and large size. FeOH colloids may also reversibly exchange with sinking organic particles, or they may be dissolved into free Fe ions (Cullen et al., 2006). These free Fe ions (Fe') may in turn form complexes with naturally-occurring organic ligands (FeL complexes), or they may undergo irreversible removal via precipitation or scavenging, after which it is assumed that this iron is not available to re-enter the dissolved pool (Fig. 3). Dissolved Fe is also removed when particle-bound FeL and FeOH deposit on the seafloor (Fig. 3). An equilibrated reversible exchange of seawater FeOH and FeL with the background biogenic particulate organic carbon (POC; represented as funnels in Fig. 3) allows hydrothermal Fe to slowly descend in the water column. In all, our model carries two dissolved Fe tracers, inorganic Fe (FeOH) and organic Fe (FeOr, which is the sum of Fe' and FeL). Additional details and model equations can be found in the Supplementary Materials.

We implemented this hydrothermal Fe model in a global steady-state ocean circulation inverse model (DeVries and Holzer,

2019). The circulation model has a resolution of 2° in the horizontal with 24 vertical levels, ranging in thickness from ~30 m near the surface to \sim 500 m in the deep ocean, and has been optimized to closely reproduce the distribution of five circulation tracers: potential temperature, salinity, radiocarbon (Δ^{14} C), CFC-11, and δ^{3} He (DeVries and Holzer, 2019). The model also provides an estimate of mantle ³He venting rates from mid-ocean ridges (DeVries and Holzer, 2019), which we use to simulate hydrothermal Fe sources using a constant Fe: ³He ratio. The modeled δ ³He shows excellent agreement with the observations along the GP16 transect (Fig. 4A; R = 0.98) and in other ocean regions (DeVries and Holzer, 2019). The circulation model is used offline to provide the physical transport of dissolved Fe in our model. We use five different variants of the model which differ in terms of their subgrid diffusivities (DeVries and Holzer, 2019), in order to estimate uncertainties introduced by ocean circulation in our model.

Our Fe model simulates the venting and dispersion of hydrothermal Fe emitted from all mid-ocean ridges, just like previous 3-dimensional global Fe models (e.g. Resing et al., 2015), but does not include Fe from any other sources. Our model has twelve uncertain parameters, and we use our size-resolved dissolved Fe data from the GP16 transect (Fig. 1) to estimate the values of these parameters where possible. Six of the parameters are specifically related to the behavior of hydrothermal Fe and can be independently constrained using our dissolved Fe observations, so we refer to these parameters as "control parameters". The other six parameters are related to the generic Fe cycle and cannot be constrained using our dissolved Fe observations, and we refer to these parameters as "hyperparameters" (see Suppl. Fig. 4). After fixing the hyperparameters at reasonable values, we used a genetic algorithm to find the set of control parameters that minimized the misfit between our modeled soluble and colloidal hydrothermal Fe, and the observations shown in Fig. 1. We repeated this optimization 64 times using the control (CTL) version of our circulation model (De-Vries and Holzer, 2019), each time using a different combination of hyperparameters that were varied within realistic ranges. We then combined these 64 different parameter sets with the five different variants of our circulation model, to produce 320 unique simulations of hydrothermal Fe. These simulations are used to report uncertainties on the quantities calculated with our model, which reflect the standard deviation across these 320 simulations. Further information on the model parameters and optimization scheme is provided in the Supplementary Material.

The optimization was able to find parameters that allow an excellent agreement between the modeled and observed Fe along the GP16 transect (Fig. 4; R = 0.88 for the mean of our 64 different optimized models). The model captures all of the main features of the observations, including the westward advection of the hydrothermal Fe plume, the vertical descent of the Fe plume, and the bimodal peak in dissolved Fe with local maxima at both 115° W and 125° W (Fig. 4B, c.f. Fig. 1B). The model fidelity to the colloidal Fe data (Fig. 4C, c.f. Fig. 1C) is better than that to the soluble Fe data (Fig. 4D, c.f. Fig. 1D), which is expected given the larger uncertainty to variability ratio associated with the soluble Fe measurements (see section 2). The model slightly underestimates soluble Fe above the core of the hydrothermal plume, while it slightly overestimates soluble Fe below the core of the plume (Fig. 4D, c.f. Fig. 1D), indicating that the settling of soluble Fe (driven by the reversible scavenging of Fe colloids and their dissolution to soluble Fe) may be slightly overestimated in the model. In all other respects the model is close to the observations.

Our model also predicts changes in the chemical speciation of hydrothermal dissolved Fe along the GP16 transect (Fig. 5). Near the hydrothermal vents along the EPR, the plume is composed primarily of inorganic FeOH that is released from the vents (Fig. 5A). A secondary maximum of FeOH at \sim 125° W indicates FeOH re-

leased from upstream vents along the EPR and circulated to the transect, a feature also seen in the δ^3 He data along this transect (Jenkins et al., 2018). West of \sim 125° W, the plume becomes dominated by organic Fe (FeOr), which comprises \sim 70-80% of the dissolved Fe in the far western part of the transect (Fig. 5B, C). At \sim 150° W, the core of the FeOH plume is found at \sim 3,000 m, about 500 m below the EPR vent depths (Fig. 5A), while the core of the FeOr plume is only slightly below 2,500 m (Fig. 5B). This indicates that the downward settling of the hydrothermal Fe plume in our model is driven primarily by FeOH. Our optimization finds that the adsorption coefficient for FeOH is roughly 10 times larger than that for FeL (Suppl. Fig. 4), which allows FeOH to be more strongly scavenged by sinking particles than FeOr, and to be brought deeper into the water column.

3.3. Fate of hydrothermal Fe released from the East Pacific Rise

Our optimized model diagnoses a Fe: 3 He ratio of 6.4 \pm 0.7 nmol Fe:fmol 3 He, which is slightly lower than the value of 7.5 \pm 0.8 nmol Fe:fmol 3 He determined by Resing et al. (2015) from their dissolved Fe measurements in the plume. Using the mantle 3 He source map of DeVries and Holzer (2019) yields a Fe hydrothermal input rate of 1.5 \pm 0.2 Gmol yr $^{-1}$ from the EPR vents (Table 1). Once released from the vents of the EPR, hydrothermal Fe is stabilized by reversible scavenging onto sinking organic particles, which aid in the distal transport of hydrothermal Fe. Our model shows that hydrothermal Fe from EPR vents is transported throughout the deep Pacific Ocean (Fig. 6A). In addition to promoting long-range transport of hydrothermal Fe away from vent locations, reversible scavenging also slowly settles hydrothermal Fe to the deep ocean, where it enters the densest waters of the deep ocean (Fig. 6B).

The settling effect of reversible scavenging can be seen by comparing the distribution of EPR-vented hydrothermal Fe in our reversible exchange model, with that from a previously-hypothesized model in which hydrothermal Fe is stabilized by organic ligands produced at hydrothermal vent sites (Resing et al., 2015; Tagliabue and Resing, 2016; Sander and Koschinsky, 2011). We implemented such a model in our ocean circulation framework, and optimized it following the same procedure as that for our reversible exchange model (see Supplementary Materials for details). Both our "reversible scavenging" model, and the previously-hypothesized "hydrothermal ligand" model, predict that hydrothermal Fe released from EPR vents can build up to significant concentrations (\sim 0.1-0.6 nmol/kg) in the deep Pacific Ocean for equivalent input rates, and can be transported across the entire basin (Fig. 6A and C). However, the hydrothermal ligand model cannot reproduce the observed descent of the hydrothermal Fe plume (Suppl. Fig. 5), and the vertical distribution of hydrothermal Fe differs from that of the reversible scavenging model (Fig. 6B and D). The hydrothermal ligand model predicts high Fe concentrations confined to mid-depths and intermediate waters (~2,500 m depth) (Fig. 6D), while the reversible scavenging model also predicts significant amounts of hydrothermal Fe in the deep ocean below 2,500 m depth (Fig. 6B).

The vertical distribution of hydrothermal Fe has important implications for how and where this Fe may ultimately reach surfacedwelling plankton and stimulate biological productivity. Intermediate waters generally have shorter transit times to the surface and upwell in multiple regions such as the equator, North Pacific, and Southern Ocean, whereas deep Pacific waters experience longer transit times to the surface and upwell almost exclusively in the Southern Ocean (DeVries and Primeau, 2011). Ultimately, of the 1.5 \pm 0.2 Gmol yr $^{-1}$ of Fe released from EPR vents, our simulations with the reversible scavenging model show that only 0.017 \pm 0.015 Gmol yr $^{-1}$ reaches the surface ocean, with roughly 90% of

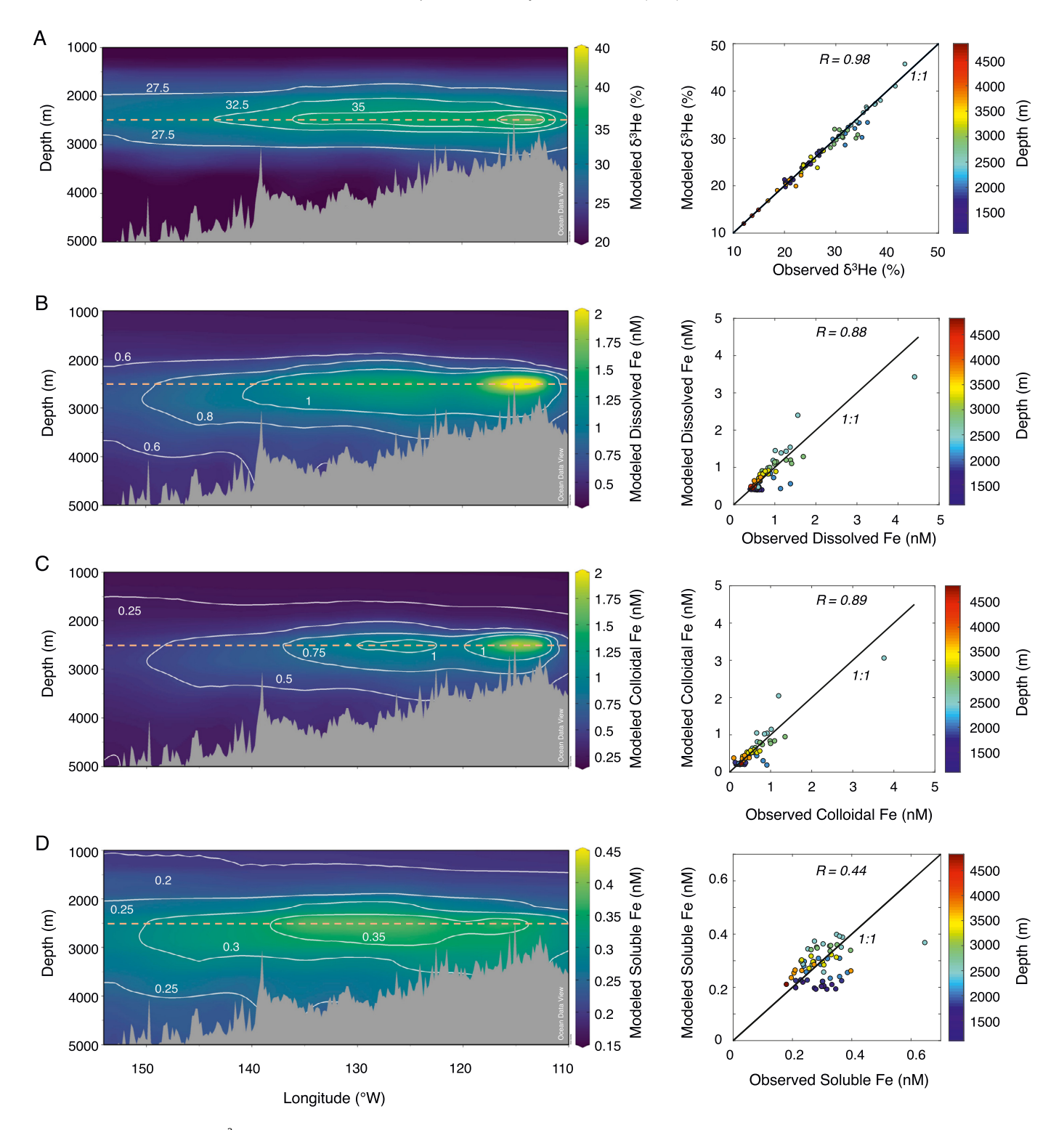


Fig. 4. Distributions of modeled δ^3 He (A), total dissolved Fe (B), colloidal Fe (C) and soluble Fe (D) along the western segment of the GP16 transect (locations shown in Fig. 1). Results are the average of 64 different optimized versions of our reversible exchange model of hydrothermal Fe. The right-hand panels in each row compare the modeled and observed (see Fig. 1) quantities along the transect, with colors indicating depth, for observations below 1,000 m. *R* values represent the correlation coefficient between modeled and observed concentrations. The model is able to reproduce both the distal transport and vertical descent of the plume, with the depth of maximum Fe concentration increasing west of the vent location at 2,500 m depth (marked by dashed orange lines). The color map settings (e.g., range and spectra) are identical to those of Fig. 1A-D. Color maps were created using Ocean Data View (Schlitzer, 2016).

this in the Southern Ocean (Table 1). The remainder is removed via various mechanisms such as precipitation or scavenging of free Fe, aggregation of FeL complexes, or burial of FeOH adsorbed onto sinking organic particles (Suppl. Table 1).

The total amount of hydrothermal Fe reaching the surface from EPR vents is two orders of magnitude smaller than Fe deposited from aeolian dust, which is \sim 6-8 Gmolyr⁻¹ (Mahowald et al., 2009; Scanza et al., 2018). In the Southern Ocean, dust deposition

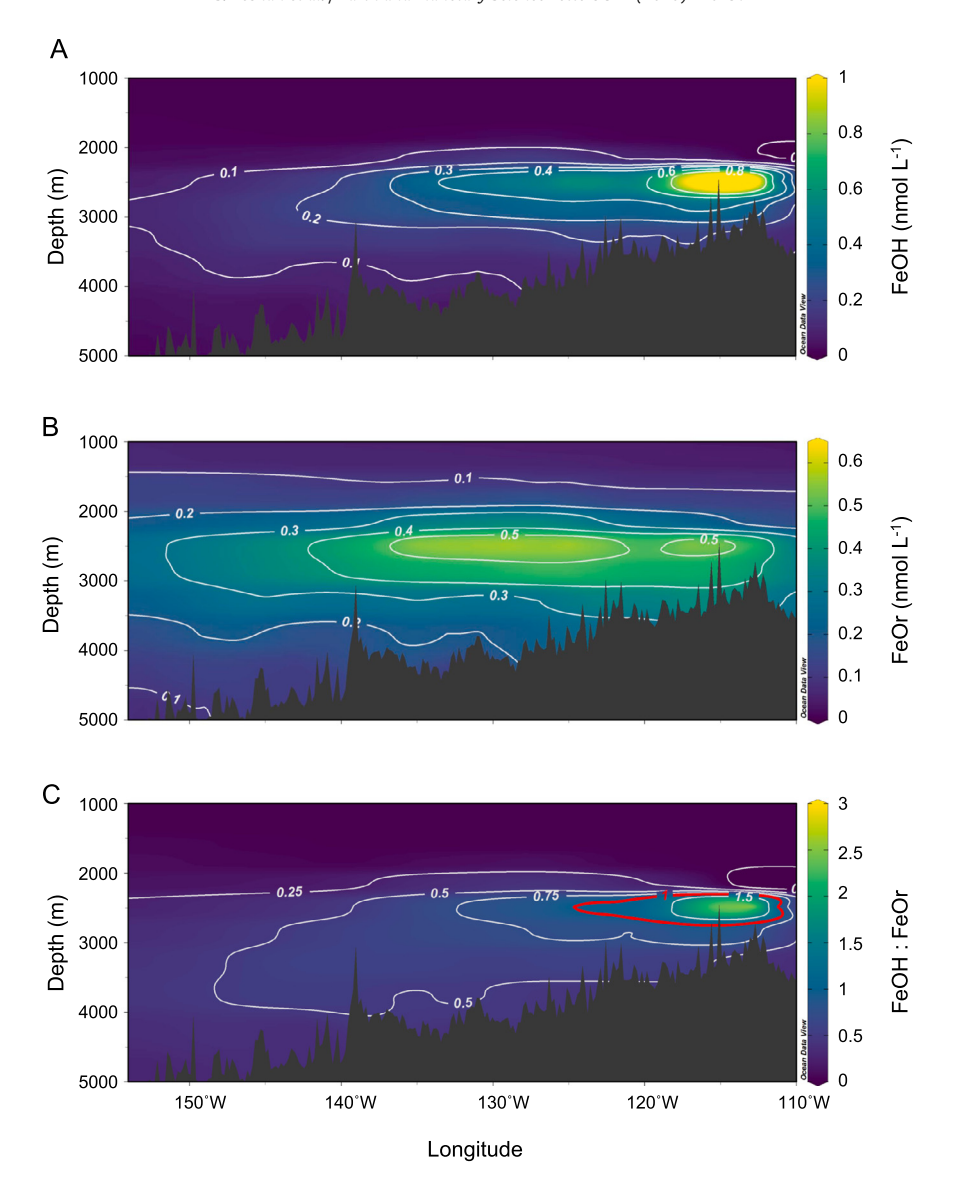


Fig. 5. Distributions of modeled (A) hydrothermal inorganic Fe (FeOH), (B) organic Fe (FeOr), and (C) the ratio of FeOH:FeOr along the western portion of the GP16 transect. The red contour in panel (C) marks a 1:1 ratio of FeOH:FeOr. Results are the average of 64 different optimized versions of our reversible exchange model of hydrothermal Fe. The model predicts that FeOH is the dominant phase near the vent, but is gradually converted (by dissolution and binding with background ligands) to FeOr further away from the vent.

Table 1Estimates of hydrothermal Fe venting rates and supply to the surface ocean in reversible exchange model.

Vent System	Venting rate (Gmol yr ⁻¹) ^a	Amount reaching surface $(Gmol yr^{-1})^b$	Percentage in the Southern Ocean ^c
East Pacific Rise	1.5 ± 0.2	0.017 ± 0.015	90 ± 9%
	0.8 ± 0.1	0.015 ± 0.012	$94 \pm 6\%$
	1.2 ± 0.4	0.016 ± 0.014	$92\pm6\%$
Southern Ocean	0.9 ± 0.1	0.05 ± 0.04	$99\pm2\%$
	2.1 ± 0.2	0.14 ± 0.07	$99 \pm 2\%$
	1.5 ± 0.6	0.10 ± 0.07	$99\pm2\%$
Global	3.9 ± 0.5	0.12 ± 0.07	82 ± 5%
	5.2 ± 0.6	0.28 ± 0.15	75 ± 7%
	4.6 ± 0.8	0.20 ± 0.14	78 ± 7%

a Based on mantle 3 He venting rates from DeVries and Holzer (2019) (top row for each vent system) and Holzer et al. (2017) (middle row for each vent system) and our optimized Fe; 3 He ratio of 6.4 ± 0.7 for SEPR ridge vents. Bottom row for each vent system is the average of the first two rows.

^b Based on 320 different simulations using our reversible exchange hydrothermal Fe model and 5 different circulation models from DeVries and Holzer (2019).

Gof the total amount of hydrothermal Fe reaching the surface, what percent reaches the surface in the Southern Ocean (south of 45° S).

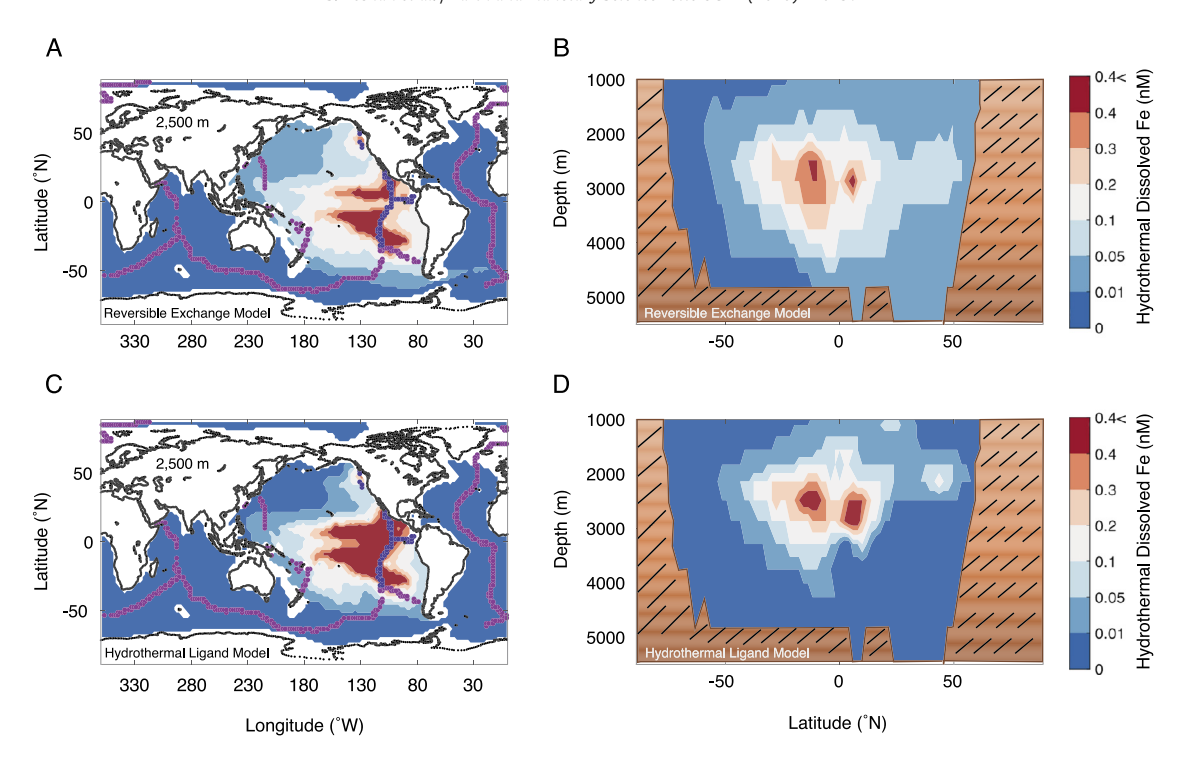


Fig. 6. Distributions of hydrothermal dissolved Fe released from the vents of the East Pacific Rise as simulated by our proposed reversible scavenging model (A and B), and by the previously hypothesized hydrothermal ligand model (C and D). Note the non-linear color scale. A and C show horizontal distributions of hydrothermal Fe at 2,500 m (the mean depth of hydrothermal Fe injection), and the locations of the East Pacific Rise (blue dots) and the rest of the global mid-ocean ridges (pink dots). B and D show basin-averaged vertical distributions of hydrothermal Fe from EPR vents in the Pacific Ocean.

supplies \sim 0.1-0.4 Gmol Fe yr⁻¹, which is still an order of magnitude larger than hydrothermal Fe from EPR vents. Overall, these results suggest a limited impact of hydrothermal Fe from EPR vents on surface biological activity.

4. Discussion

Our new model of hydrothermal Fe dispersion can be used to estimate the global supply of hydrothermal Fe to the surface ocean, keeping in mind the uncertainties associated with scaling a model optimized using data from one particular ridge system to the global scale. The global supply of hydrothermal Fe to the surface ocean depends on a wide variety of factors, including the rate and pattern of hydrothermal Fe input, the stabilization and scavenging of hydrothermal Fe, and the circulation and ventilation of the deep ocean. The circulation and ventilation of the deep ocean is well-constrained in the suite of ocean circulation inverse models used here (DeVries and Holzer, 2019), and our models that were optimized against the size-resolved Fe data from the GP16 transect provide strong constraints on the stabilization and scavenging of hydrothermal Fe, assuming that the behavior of the SEPR plume is representative of hydrothermal Fe plumes in other basins.

The rate and pattern of hydrothermal Fe input is by far the largest unknown in scaling our results to the global scale. In our model and in other marine Fe cycle models (e.g. Resing et al., 2015; Tagliabue et al., 2014), the hydrothermal Fe input is parameterized using a Fe: He venting ratio multiplied by the He input at each individual vent site. Although the Fe: He ratio along the SEPR is well constrained at \sim 6.4 nmol: fmol in our model, different ridge systems may have different Fe: He ratios in their vent fluids. Indeed, ratios as high as 70 \pm 30 nmol: fmol have been suggested for vents in the South Atlantic (Saito et al., 2013), while lower ratios of 1.5 nmol: fmol have been inferred for some Southern Ocean vents (Tagliabue et al., 2010). The extremely high Fe: He ratios found in the Atlantic Ocean (Saito et al., 2013) are probably not applicable for global models such as ours, since those num-

bers were derived from measurements very close to the vent site, and these ratios cannot be extrapolated to coarse-resolution models that do not simulate the near-field dynamics of Fe scavenging and precipitation. Here, we apply a uniform Fe:3He ratio derived from the SEPR vent system globally, with the understanding that there are likely large-scale spatial variations of at least a factor of two in this number. For the hydrothermal ³He input field we use the map of DeVries and Holzer (2019), which is designed to be consistent with the observed δ^3 He distribution and yields a global 3 He input of \sim 600 mol yr $^{-1}$, similar to a previous data-based estimate (Bianchi et al., 2010). As a measure of uncertainty, we also apply the mantle ³He input field of Holzer et al. (2017), which has a slightly larger global 3 He input of \sim 800 mol yr $^{-1}$, with substantially more 3 He input from Southern Ocean ridges (\sim 350 mol yr $^{-1}$ compared to \sim 150 mol yr⁻¹ in the estimate of DeVries and Holzer (2019)).

In all, we perform 640 different global hydrothermal Fe simulations with our model, by combining our 64 different optimized hydrothermal Fe models (Section 3.3) with five different circulation models from DeVries and Holzer (2019) and two different mantle $^3{\rm He}$ input maps from DeVries and Holzer (2019) and Holzer et al. (2017). Using the $^3{\rm He}$ input map of DeVries and Holzer (2019) yields a global hydrothermal Fe input of 3.9 \pm 0.5 Gmol yr $^{-1}$, while using the larger $^3{\rm He}$ input rates from Holzer et al. (2017) yields a global hydrothermal Fe source of 5.2 \pm 0.6 Gmol yr $^{-1}$. These values are within the range of previous estimates for the global dissolved Fe source from hydrothermal vents (1 to 11 Gmol yr $^{-1}$) (Resing et al., 2015; Tagliabue and Resing, 2016; Tagliabue et al., 2010).

The amount of hydrothermal Fe reaching the surface is roughly 0.12-0.28 Gmol yr⁻¹, which represents about 3-5% of the total hydrothermal Fe venting rate, depending on the mantle ³He input map used in the model (Table 1). About 80% of hydrothermal Fe from global ridge systems that reaches the surface does so in the Southern Ocean, with the rest reaching the surface primarily in the North Pacific and North Atlantic (Fig. 7A). A significant portion

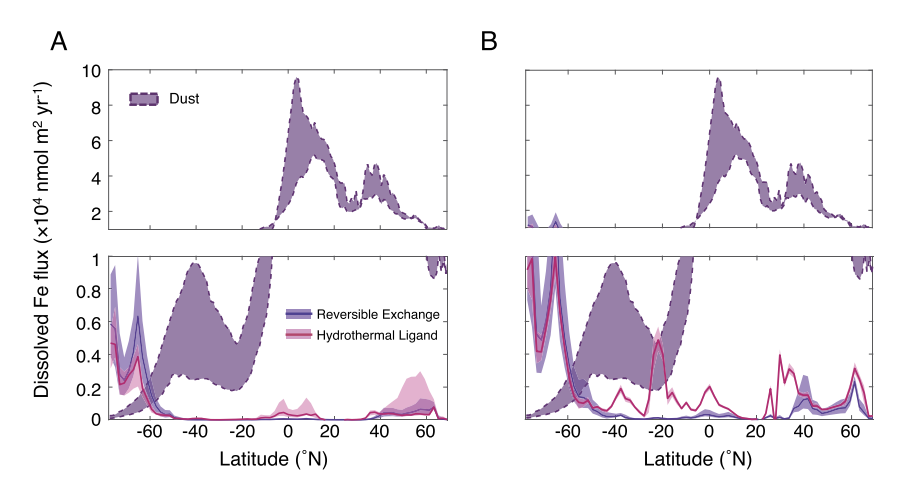


Fig. 7. Supply rate of hydrothermal Fe to the surface ocean derived from applying the global ³He sourcing maps of DeVries and Holzer (2019) (A) and Holzer et al. (2017) (B), and a constant Fe: ³He ratio using the models discussed in the text: reversible scavenging model (blue solid line and shading represent median and interquartile range of 320 model simulations) and hydrothermal ligand model (pink solid line and shading represent median and interquartile range of 320 model simulations), Shown for comparison is the zonally-averaged flux of dissolved Fe from atmospheric dust (aerosol) deposition (purple patch; adapted from Mahowald et al., 2009 and Scanza et al., 2018).

of the hydrothermal Fe that reaches the surface ocean originates from Southern Ocean ridge systems, while the ridge systems of the EPR play a negligible role in supplying hydrothermal Fe to the surface, even though they account for $\sim\!25\%$ of the global hydrothermal Fe source (Table 1). Our model simulations predict that 0.16 \pm 0.11 Gmol yr $^{-1}$ of hydrothermal Fe makes it to the Southern Ocean surface, which is almost equivalent to the supply of Fe from dust deposition in the Southern Ocean (0.1-0.4 Gmol yr $^{-1}$). These results are consistent with observations demonstrating that algal blooms can be triggered by upwelling of hydrothermal Fe in the Southern Ocean (Ardyna et al., 2019). Outside of the Southern Ocean, the supply of hydrothermal Fe to the surface ocean is negligible compared to the supply of Fe from aerosol dust (Fig. 7).

It is interesting to contrast the rates and patterns of hydrothermal Fe supply to the surface in our reversible scavenging model with the previously-hypothesized hydrothermal ligand model. In the hydrothermal ligand model, about 4-7% of hydrothermal Fe makes it to the surface (Suppl. Table 2 and Suppl. Table 3), compared with 3-5% in the reversible scavenging model. However, only \sim 40% of the Fe in the hydrothermal ligand model reaches the surface in the Southern Ocean (Suppl. Table 3). The overall effect is that there is 25% less hydrothermal Fe reaching the Southern Ocean surface in the hydrothermal ligand model compared to the reversible scavenging model (Fig. 7). This difference is tied to the downward settling of hydrothermal Fe in the reversible scavenging model, which causes the Fe to become trapped in dense deep water masses that preferentially outcrop in the Antarctic region of the Southern Ocean. In the hydrothermal ligand model, the Fe vented from mid-ocean ridges does not settle into the deep ocean, and significant amounts reach the surface outside of the Southern Ocean in the tropics and northern high latitudes (Fig. 7).

It is beyond the scope of this study to determine the impact of hydrothermal Fe on carbon export in the Southern Ocean, as this depends in complex ways on the relative supply of Fe from other sources and the spatial distribution of each source (Wadley et al., 2014). Our simulations suggest that the supply of hydrothermal Fe to the Southern Ocean surface rivals that of Fe from aerosol dust deposition, but with a spatial distribution that is more concentrated in the Antarctic region south of the polar front (\sim 55° S), due to the predominance of deep water upwelling in this region (Fig. 7). The small spatial extent of hydrothermal Fe in the Southern Ocean could ultimately limit its impact on carbon export, as demonstrated by the modeling study of Tagliabue and Resing (2016). Furthermore, other regional sources of Fe from the melting of icebergs, glaciers, and sea ice (Death et al., 2014; Laufkötter

et al., 2018), as well as Fe released from shelf sediments (Wadley et al., 2014), could render hydrothermal Fe less important in this region.

5. Conclusion

Here, we presented new observations of the size speciation of dissolved Fe in a basin-scale hydrothermal plume in the Southeast Pacific, and proposed a new mechanistic model to explain these data. In this model, Fe is released from hydrothermal vents as large inorganic colloids, and is gradually transformed to organic forms further away from the vents. Reversible scavenging of inorganic Fe colloids drives a gradual downward settling of hydrothermal Fe, leading to the accumulation of hydrothermal Fe in dense deep-sea water masses. Unlike previous studies in which the stabilization of hydrothermal Fe was explained by the release of ligands from hydrothermal vents, our model can recreate both the observed lateral extent and downward settling of the hydrothermal plume. When implemented in a global data-constrained circulation model, our new model of hydrothermal Fe dispersion demonstrates that hydrothermal Fe can build up to high concentrations in the deep ocean (reaching \sim 0.2-0.4 nM in the deep Pacific Ocean; Suppl. Fig. 6), but only \sim 3-5% of hydrothermal Fe ever makes it to the surface ocean. Furthermore, the surface impact of hydrothermal Fe is confined to the Antarctic region of the Southern Ocean where the densest water masses outcrop.

These results suggest several avenues for further research that can help to better understand the role of hydrothermal Fe in the global marine Fe cycle. First, in order to provide stronger constraints on models of hydrothermal dispersion, it will be important to characterize the size speciation and chemical composition of Fe in other large-scale hydrothermal plumes (e.g., Lough et al., 2019; Cotte et al., 2020). Given the success of the reversible scavenging model at reproducing the observed downward settling of hydrothermal Fe in the Southeast Pacific, future observational studies should examine the ubiquity of reversible scavenging of Fe in the ocean, and whether the scavenging of Fe in the ocean (Tagliabue et al., 2019; Ohnemus et al., 2019) can be more generally modeled as reversible like for other trace metals such as copper (Little et al., 2013; Richon and Tagliabue, 2019) and zinc (Weber et al., 2018). Furthermore, given the dominance of Southern Ocean ridge systems in supplying hydrothermal Fe to the surface ocean, studies should be performed to determine the rate of Fe venting from Southern Ocean ridges, and to constrain the Fe:³He ratio at different locations along the Southern Ocean ridge system. Lastly, the

reversible scavenging model of hydrothermal Fe should be implemented in global biogeochemical models, to examine the impact of hydrothermal Fe on carbon export in the Southern Ocean.

Declaration of competing interest

The authors declare that they have no known competing financial interests or personal relationships that could have appeared to influence the work reported in this paper.

Acknowledgements

We thank the captain and crew of the RV *Thompson*, and chief scientists and sampling team of GEOTRACES GP16 cruise. We also thank Gedun Chen for help in laboratory analyses. This work was supported by the US National Science Foundation with grants OCE-1658392 to T.D., OCE-1233155 to J.W., OCE-1658436 to S.J., and OCE-1658042 to T.W.

Appendix A. Supplementary material

Supplementary material related to this article can be found online at https://doi.org/10.1016/j.epsl.2020.116297.

References

- Abualhaija, M.M., Whitby, H., van den Berg, C.M., 2015. Competition between copper and iron for humic ligands in estuarine waters. Mar. Chem. 172, 46–56.
- Ardyna, M., Lacour, L., Sergi, S., d'Ovidio, F., Sallée, J.B., Rembauville, M., Blain, S., Tagliabue, A., Schlitzer, R., Jeandel, C., Arrigo, K.R., 2019. Hydrothermal vents trigger massive phytoplankton blooms in the Southern Ocean. Nat. Commun. 10, 2451.
- Bianchi, D., Sarmeinto, J.L., Gnandesikan, A., Key, R.M., Schlosser, P., Newton, R., 2010. Low helium flux from the mantle inferred from simulations of oceanic helium isotope data. Earth Planet. Sci. Lett. 297 (3–4), 379–386.
- Boyd, P.W., Jickells, T., Law, C.S., Blain, S., Boyle, E.A., Buesseler, K.O., Coale, K.H., Cullen, J.J., De Baar, H.J., Follows, M., Harvey, M., 2007. Mesoscale iron enrichment experiments 1993–2005: synthesis and future directions. Science 315, 612–617.
- Cullen, J.T., Bergquist, B.A., Moffett, J.W., 2006. Thermodynamic characterization of the partitioning of iron between soluble and colloidal species in the Atlantic Ocean. Mar. Chem. 98, 295–303.
- Cotte, L., Chavagnac, V., Pelleter, E., Laës-Huon, A., Cathalot, C., Dulaquais, G., Riso, R.D., Sarradin, P.-M., Waeles, M., 2020. Metal partitioning after in situ filtration at deep-sea vents of the Lucky Strike hydrothermal field (EMSO-Azores, Mid-Atlantic Ridge, 37° N). Deep-Sea Res., Part 1, Oceanogr. Res. Pap. 157, 103204.
- Death, R., Wadham, J.L., Monteiro, F., Le Brocq, A.M., Tranter, M., Ridgwell, A., Dutkiewicz, S., Raiswell, R., 2014. Antarctic ice sheet fertilises the Southern Ocean. Biogeosciences 11, 2635–2643.
- DeVries, T., Primeau, F., 2011. Dynamically and observationally constrained estimates of water-mass distributions and ages in the global ocean. J. Phys. Oceanogr. 41, 2381–2401.
- DeVries, T., Holzer, M., 2019. Radiocarbon and helium isotope constraints on deep ocean ventilation and mantle-³He sources. J. Geophys. Res., Oceans 124, 1–22.
- Feely, R.A., Baker, E.T., Marumo, K., Urabe, T., Ishibashi, J., Gendron, J., Lebon, G.T., Okamura, K., 1996. Hydrothermal plume particles and dissolved phosphate over the superfast-spreading southern East Pacific Rise. Geochim. Cosmochim. Acta 60, 2297–2323.
- Fitzsimmons, J.N., John, S.G., Marsay, C.M., Hoffman, C.L., Nicholas, S.L., Toner, B.M., German, C.R., Sherrell, R.M., 2017. Iron persistence in a distal hydrothermal plume supported by dissolved-particulate exchange. Nat. Geosci. 10, 195.
- Fitzsimmons, J.N., Boyle, E.A., Jenkins, W.J., 2014. Distal transport of dissolved hydrothermal iron in the deep South Pacific Ocean. Proc. Natl. Acad. Sci. USA 111, 16654–16661.
- Hoffman, C.L., Nicholas, S.L., Ohnemus, D.C., Fitzsimmons, J.N., Sherrell, R.M., German, C.R., Heller, M.I., Lee, J.M., Lam, P.J., Toner, B.M., 2018. Near-field iron and carbon chemistry of non-buoyant hydrothermal plume particles, Southern East Pacific Rise 15° S. Mar. Chem. 201, 183–197.
- Holzer, M., DeVries, T., Bianchi, D., Newton, R., Schlosser, P., Winckler, G., 2017. Objective estimates of mantle 3He in the ocean and implications for constraining the deep ocean circulation. Earth Planet. Sci. Lett. 458, 305–314.
- Jenkins, W.J., Lott III, D.E., German, C.R., Cahill, K.L., Goudreau, J., Longworth, B., 2018. The deep distributions of helium isotopes, radiocarbon, and noble gases

- along the US GEOTRACES East Pacific Zonal Transect (GP16). Mar. Chem. 201, 167-182
- Laufkötter, C., Stern, A.A., John, J.G., Stock, C.A., Dunne, J.P., 2018. Glacial iron sources stimulate the Southern Ocean carbon cycle. Geophys. Res. Lett. 45, 13377–13385.
- Little, S.H., Vance, D., Siddall, M., Gasson, E., 2013. A modeling assessment of the role of reversible scavenging in controlling oceanic dissolved Cu and Zn distributions. Glob. Biogeochem. Cycles 27, 780–791.
- Lough, A.J.M., Homoky, W.B., Connelly, D.P., Comer-Warner, S.A., Nakamura, K., Abyaneh, M.K., Kaulich, B., Mills, R.A., 2019. Soluble iron conservation and colloidal iron dynamics in a hydrothermal plume. Chem. Geol. 511, 225–237.
- Mahowald, N.M., Engelstaedter, S., Luo, C., Sealy, A., Artaxo, P., Benitez-Nelson, C., Bonnet, S., Chen, Y., Chuang, P.Y., Cohen, D.D., Dulac, F., 2009. Atmospheric iron deposition: global distribution, variability and human perturbations. Annu. Rev. Mar. Sci. 1, 245–278.
- Martell, A.E., Smith, R.M., 2013. Critical Stability Constants: First Supplement (Vol. 5). Springer Science & Business Media, New York.
- Moffett, J.W., German, C.R., 2018. The US GEOTRACES Eastern Tropical Pacific Transect (GP16). Mar. Chem. 201, 1–5.
- Moore, C.M., Mills, M.M., Arrigo, K.R., Berman-Frank, I., Bopp, L., Boyd, P.W., Galbraith, E.D., Geider, R.J., Guieu, C., Jaccard, S.L., Jickells, T.D., 2013. Processes and patterns of oceanic nutrient limitation. Nat. Geosci. 6, 701–710.
- Ohnemus, D.C., Torrie, R., Twining, B.S., 2019. Exposing the distributions and elemental associations of scavenged particulate phases in the ocean using basin-scale multi-element data sets. Glob. Biogeochem. Cycles 33 (6), 725–748.
- Resing, J.A., Sedwick, P.N., German, C.R., Jenkins, W.J., Moffett, J.W., Sohst, B.M., Tagliabue, A., 2015. Basin-scale transport of hydrothermal dissolved metals across the South Pacific Ocean. Nature 523, 200–203.
- Richon, C., Tagliabue, A., 2019. Insights into the major processes driving the global distribution of copper in the ocean from a global model. Glob. Biogeochem. Cycles 32 (12), 1594–1610.
- Roshan, S., Wu, J., 2018. Dissolved and colloidal copper in the tropical South Pacific. Geochim. Cosmochim. Acta 233, 81–94.
- Rudnicki, M.D., Elderfield, H., 1993. A chemical model of the buoyant and neutrally buoyant plume above the TAG vent field, 26 degrees N, Mid-Atlantic Ridge. Geochim. Cosmochim. Acta 57 (13), 2939–2957.
- Saito, M.A., Noble, A.E., Tagliabue, A., Goepfert, T.J., Lamborg, C.H., Jenkins, W.J., 2013. Slow-spreading submarine ridges in the South Atlantic as a significant oceanic iron source. Nat. Geosci. 6, 775–779.
- Sander, S.G., Koschinsky, A., 2011. Metal flux from hydrothermal vents increased by organic complexation. Nat. Geosci. 4, 145–150.
- Scanza, R.A., Hamilton, D.S., Perez Garcia-Pando, C., Buck, C., Baker, A., Mahowald, N.M., 2018. Atmospheric processing of iron in mineral and combustion aerosols: development of an intermediate-complexity mechanism suitable for Earth system models. Atmos. Chem. Phys. 18, 14175–14196.
- Schlitzer, R., 2016. Ocean data view. http://odv.awi.de.
- Stommel, H., 1982. Is the South Pacific helium-3 plume dynamically active?. Earth Planet. Sci. Lett. 61 (1), 63–67.
- Stumm, W., Morgan, J.J., 1996. Aquatic Chemistry. John Wiley & Sons Inc., New York. Tagliabue, A., et al., 2010. Hydrothermal contribution to the oceanic dissolved iron inventory. Nat. Geosci. 3, 252–256.
- Tagliabue, A., Aumont, O., Bopp, L., 2014. The impact of different external sources of iron on the global carbon cycle. Geophys. Res. Lett. 41, 920–926.
- Tagliabue, A., Aumont, O., DeAth, R., Dunne, J.P., Dutkiewicz, S., Galbraith, E., Misumi, K., Moore, J.K., Ridgwell, A., Sherman, E., Stock, C., 2016. How well do global ocean biogeochemistry models simulate dissolved iron distributions? Glob. Biogeochem. Cycles 30, 149–174.
- Tagliabue, A., Resing, J., 2016. Impact of hydrothermalism on the ocean iron cycle. Phil. Trans. R. Soc. A 374, 20150291.
- Tagliabue, A., Bowie, A.R., Boyd, P.W., Buck, K.N., Johnson, K.S., Saito, M.A., 2017. The integral role of iron in ocean biogeochemistry. Nature 543, 51–59.
- Tagliabue, A., Bowie, A.R., DeVries, T., Ellwood, M.J., Landing, W.M., Milne, A., Ohnemus, D., Twining, B., Boyd, P.W., 2019. The interplay between regeneration and scavenging fluxes drives ocean iron cycling. Nat. Commun. 10 (1), 1–8.
- Wadley, M.R., Jickells, T.D., Heywood, K.J., 2014. The role of iron sources and transport for Southern Ocean productivity. Deep-Sea Res., Part 1, Oceanogr. Res. Pap. 87, 82–94.
- Weber, T., John, S., Tagliabue, A., DeVries, T., 2018. Biological uptake and reversible scavenging of zinc in the global ocean. Science 361 (6397), 72–76.
- Wu, J., Boyle, E.A., 1998. Determination of iron in seawater by high-resolution isotope dilution inductively coupled plasma mass spectrometry after Mg (OH)2 coprecipitation. Anal. Chim. Acta 367, 183–191.
- Wu, J., Roshan, S., Chen, G., 2014. The distribution of dissolved manganese in the tropical–subtropical North Atlantic during US GEOTRACES 2010 and 2011 cruises. Mar. Chem. 166, 9–24.
- Yücel, M., Gartman, A., Chan, C.S., Luther III, G.W., 2011. Hydrothermal vents as a kinetically stable source of iron-sulphide-bearing nanoparticles to the ocean. Nat. Geosci. 4, 367–371.